International Journal of Hydrogen Energy 101 (2025) 303–312

Contents lists available at ScienceDirect

International Journal of Hydrogen Energy

journal homepage: www.elsevier.com/locate/he

Prediction and mechanism of underground hydrogen storage in nanoporous media: Coupling molecular simulation, pore-scale simulation and machine learning

Han Wang [a], Ke Hu [b], Weipeng Fan [c], Mingshan Zhang [d], Xuanzhe Xia [a], Jianchao Cai [a,*]

[a] State Key Laboratory of Petroleum Resources and Engineering, China University of Petroleum, Beijing, 102249, China
[b] Civil and Environmental Engineering Department, University of Alberta, Edmonton, T6G 1H9, Canada
[c] CNOOC Research Institute Ltd, Beijing, 100028, China
[d] Key Laboratory of Ministry of Education on Safe Mining of Deep Metal Mines, School of Resources and Civil Engineering, Northeastern University, Shenyang, 110819, China

ARTICLE INFO

Handling Editor: Dr J Ortiz

Keywords:
Underground hydrogen storage
Molecular simulation
Machine learning
Shale nanoporous media
Lattice Boltzmann model

ABSTRACT

The strong adsorption of hydrogen (H_2) in nanoscale space resulting from non-negligible gas-solid interaction greatly impacts underground H_2 storage and recovery efficiency in shale reservoirs. Clarifying H_2 adsorption behaviors from a microscopic perspective is crucial for advancing a green and low-carbon economy. However, molecular simulations of adsorption behaviors are limited to the single nanopores ignoring complex pore structures, while pore-scale simulations suffer from accuracy issues and high computational resource demands. This paper presents a methodology that integrates molecular simulation, pore-scale simulation, and machine learning to simulate and predict the density distribution of gas in nanoporous media. First, an improved lattice Boltzmann model is developed by incorporating a source term condition into the bulk region, coupled with density distribution from molecular simulations, to accurately and efficiently calculate the H_2 density distribution in various nanoporous media under specific temperature and pressure conditions in a single simulation. Second, 2538 pore structures from various nanoporous media are extracted using the watershed algorithm. The features of these pore structures and the gas mass within each pore structure are then calculated. Considering 6 pressures, and 2 types of minerals (kerogen and montmorillonite), a total of 30456 machine learning data sets are generated. Subsequently, an artificial neural network is successfully trained to predict the gas mass in arbitrary pore structure with a high coefficient of determination and minimal root mean square error. Finally, utilizing the trained artificial neural network, the H_2 storage capacity in a shale kerogen digital core with 5419 pore structures is rapidly predicted, showing the mass of adsorbed gas accounted for 70.48% of the total gas mass. This model is versatile and applicable to various fluid adsorption behaviors in nanoscale environments, including shale oil/gas adsorption, CO_2 adsorption, and H_2 adsorption, which has significant implications for enhancing oil and gas recovery and promoting a green low-carbon economy.

1. Introduction

Burning fossil fuels in various industrial activities contributes to approximately 74% of greenhouse gas emissions, significantly impacting global warming and climate change [1,2]. Conversely, due to its high energy carrier and combustion only generating water, hydrogen (H_2) has emerged as a promising avenue for converting fossil fuels to environmentally friendly and low-carbon energy resources. The European Green Deal prioritizes clean H_2 as a key area to achieve net-zero greenhouse gas emissions by 2050 [3]. However, compared to methane (CH_4), the storage of H_2 necessitates a larger volume because of the lower volume/energy density, posing challenges in meeting energy storage demands [4]. Underground hydrogen storage (UHS) in depleted reservoirs presents an effective solution to the considerable challenges of H_2 storage, which is achieved through trapping by stratigraphic structure, pore space, multiphase capillary force, dissolution, adsorption, mineral trapping, microbial interactions, etc [5–12]. Among the methods of UHS, because of the high specific surface area and

* Corresponding author.
E-mail address: caijc@cup.edu.cn (J. Cai).

https://doi.org/10.1016/j.ijhydene.2024.12.406
Received 23 June 2024; Received in revised form 6 November 2024; Accepted 23 December 2024
Available online 31 December 2024

adsorption behaviors in nanoscale pore space, the depleted shale reservoirs can effectively store a large amount of H_2 [13,14]. Additionally, shale can act as an effective sealing layer, preventing H_2 leakage [15], with up to 73% of the injected H_2 can be withdrawn through depressurization [16]. As a result, the high storage and withdrawal capacity of depleted shale reservoirs makes them a potential approach for H_2 storage in depleted reservoirs. Due to the similar size of gas molecules and pores in shale reservoirs, the strong adsorption characteristics are significantly influenced by the non-negligible gas-mineral molecular interactions, which greatly affect H_2 storage capacity. However, unlike the beneficial adsorption effects on the permanent storage of CO_2, although H_2 adsorption can enhance H_2 storage capacity, it is not conducive to H_2 release [17,18]. Therefore, it is essential to study the adsorption behavior of H_2 from the microscopic perspective.

Currently, macroscopic adsorption behaviors of gases (H_2, CO_2, CH_4) in shale nanopores have been explored through experiments and numerical simulations [19–21]. Liu et al., 2019 studied CO_2–CH_4 competitive adsorption using low-field Nuclear Magnetic Resonance (NMR). Under a fixed CH_4 pressure of 3 MPa and varying CO_2/CH_4 pressure ratios, they observed that the adsorption capacity of CH_4 decreases from approximately 1 cm^3/g to 0.3 cm^3/g as the pressure ratio increases from about 1 to 2, due to the significant competitive adsorption of CO_2 [22]. Klewiah et al., 2020 provided a comprehensive review of experimental research on CO_2–CH_4 adsorption in shale, highlighting the significant influences of mineral types, kerogen maturity, and pressure [23]. Abid et al., 2022 applied a PCTpro analyzer to measure the adsorption capacities of H_2 and CH_4 in shale, and the results revealed that the H_2 adsorption increases by approximately 170% at 2.5 MPa and 350 % at 4.28 MPa at 303 K, with adsorption trends following type IV isotherm curves [24]. Alanazi et al., 2023 analyzed the effects of total organic content (TOC = 13%–18%) and pressure (0.1–10 MPa) on H_2, CO_2, and CH_4 adsorption in actual Jordanian source rocks [25]. The findings revealed a noteworthy reduction in H_2 adsorption compared to CO_2 and CH_4 as TOC increases, with H_2 adsorption decreasing from 0.5 mol/kg to 0.18 mol/kg at 9 MPa for the lowest and highest TOC. Wang et al., 2024 performed H_2 adsorption and diffusion experiments in shale samples at high pressure and elevated temperatures [26]. They reported that the H_2 adsorption amounts to approximately 65%–80% of CH_4 adsorption, with adsorption capacity positively correlated with pressure and negatively correlated with temperature. Liu et al., 2024 utilized the Computer Modeling Group to simulate H_2 storage in a depleted shale gas reservoir [16]. They found that after five injection/withdrawal cycles, the average recovery reached 22%, with approximately 73% of the injected H_2 being recoverable in the fifth cycle. Singh, 2022 adopted a numerical approach to investigate the H_2 storage capacity in depleted horizontal shale gas wells [27], discussing the effects of cycle duration (injection and production) on H_2 recovery and purity. The results indicated that the H_2 recovery increases and purity decreases with cycle duration, attributed to the increasing injected cumulative H_2 and the similar in-place cumulative H_2 after production. Additionally, the H_2 purity decreases with cycle duration possibly reason of the geological and non-geological parameters. However, macroscopic experiments and numerical simulations capture only macroscopic adsorption characteristics and cannot analyze the mechanisms of multifactor influences on adsorption from a microscopic perspective.

Instead, molecular simulation (MS) can model adsorption behaviors in nanopores, enabling analysis of the adsorption mechanisms from the perspective of molecular interaction forces [28–32]. Ho et al., 2024 investigated the H_2–CH_4 adsorption in Duvernay shale and Berea sandstone using NMR and MS [18]. NMR experiments revealed the presence of both free and adsorbed H_2 in shale, while only free gas is detected in sandstone, with approximately 10% H_2 lost due to adsorption/desorption behaviors. These observations were subsequently explained effectively by MS. Wang et al., 2023 applied the reservoir-scale simulations to explore H_2 storage capacity in shale reservoirs, based on the thermodynamics and transport mechanisms of H_2 in nanopores derived from MS. The results revealed that H_2 shows a preference for greater storage in unconventional reservoirs due to the adsorption effect, in contrast to conventional reservoirs [33]. Raza et al., 2023 employed a molecular parallel simulator (LAMMPS) to investigate H_2 adsorption in organic matter, accounting for the effects of CH_4, pressure and temperature, showing that the adsorption is influenced by these factors, with the Langmuir model effectively predicting H_2 adsorption [34]. Zhang et al., 2024 employed Grand Canonical Monte Carlo (GCMC) simulations to model H_2 and cushion gas adsorption in kerogen and montmorillonite (MMT) nanopores. The results indicated that the excess adsorption of H_2 in kerogen nanopores is approximately 2 times as large as in MMT nanopores, thereby affecting the storage capacity [17]. Shang et al., 2024 applied GCMC and molecular dynamics simulations (MDS) to investigate the dependence of H_2 adsorption behavior on pore size (1–20 nm), pressure (up to 30 MPa), and temperature (303–423 K). Deng et al., 2022 investigated the adsorption of H_2 in calcite silt nanopores applying GCMC and MDS, and the density distribution of pure H_2 shows that the peak density of adsorption H_2 is about 2.5 times that of the bulk density [35]. The results suggested that the shale reservoirs are more favorable for UHS with pore size larger than 5 nm, lower temperatures, and higher pressures [36]. However, due to the complex pore structures and diverse mineral types in shale reservoirs, the research on H_2 adsorption behavior in single nanopores based on MS may not fully reflect the influence of complex pore structures, such as varying nanopore shapes and high adsorption capacity in mineral corners [37,38].

Pore-scale simulation can effectively overcome the limitations of small computing domains through MS [39]. Lattice Boltzmann method (LBM), a popular pore-scale simulation method, is extensively employed to simulate complex fluid behaviors in intricate pore structures [39–41]. Zhao et al., 2016 established a microscale lattice Boltzmann (LB) model that incorporates adsorption behavior by integrating the density distribution from the GCMC method, and simulated gas production in shale porous media considering the adsorption effects [42]. Zhang et al., 2020 developed an innovative LBM to characterize the heterogeneous density distribution and slip flow behaviors in nanopores by incorporating intermolecular interactions [43]. Zhang et al., 2023 further improved LBM to model the adsorption behaviors in porous media. Their findings indicated that conventional adsorption theories, which are appropriate for simple pore structures, are inadequate for complex pore structures in porous media [38]. Recently, Wang et al., 2024 utilized a new LBM with modified gas-solid interaction forces to simulate CO_2–CH_4 competitive adsorption in three-dimensional (3D) nanoporous media [44,45]. However, this method cannot guarantee that the simulated CO_2–CH_4 density in the bulk phase matches the density at different temperatures/pressures and CO_2–CH_4 molar fractions, necessitating multiple adjustments to the initial CO_2–CH_4 density.

Furthermore, while LBM effectively captures intricate fluid behaviors, it is primarily utilized for qualitative analysis of fluid behaviors in two-dimensional (2D) porous media. Due to limitations in computing resources, LBM is not well-suited for quantitative calculations in 3D porous media [46]. Through coupling pore-scale simulation with machine learning, fluid behaviors in 3D porous media can be calculated accurately and rapidly [47,48]. Rabbani and Babaei, 2019 accurately computed fluid flow in pores with various cross-sectional shapes using LBM, and subsequently integrated machine learning techniques and a pore network model to enable rapid and accurate calculation of porous media permeability, achieving a coefficient of determination R^2 around 0.997 [47]. Jiang et al., 2021 introduced a methodology aimed at predicting the multiphase permeability, considering the viscous coupling effect, by integrating direct pore-scale simulation and machine learning. The results demonstrated that the trained artificial neural network (ANN) achieves a coefficient of determination R^2 higher than 0.99, indicating excellent capability in predicting permeability [48]. Kang et al., 2024 employed LBM to calculate permeability for 1000 sets of porous media, and then used a pore network model to identify 6

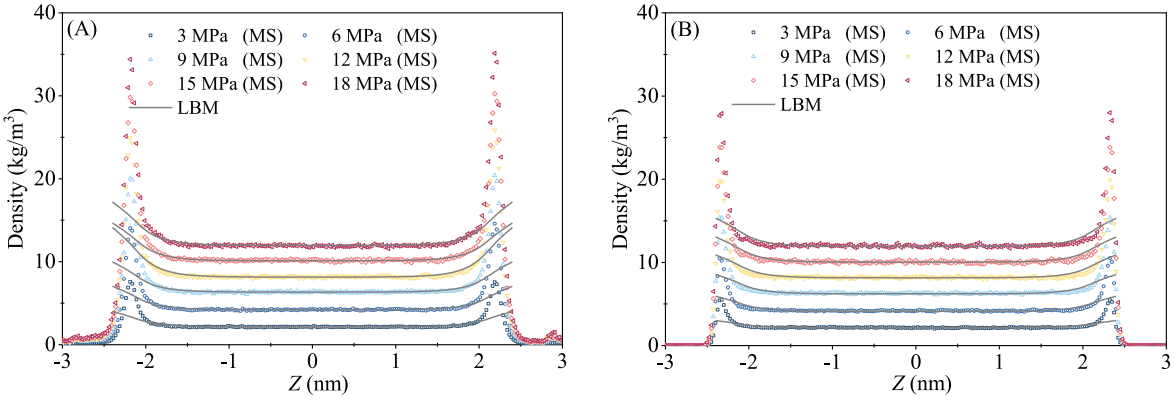

Fig. 1. LB parameters from MS density distributions. (A) Kerogen, (B) MMT. $Z = 0$ denotes the position at the middle of the pore.

characteristic parameters [49]. Leveraging this dataset, they applied machine learning techniques to predict the permeability of porous media achieving a coefficient of determination R^2 higher than 0.9. This approach improves prediction accuracy by 15% compared to empirical formulas. In addition to the machine learning based on microscopic simulation results, Thanh et al., 2024 introduced a novel approach utilizing machine learning algorithms trained on 570 experimental data samples to accurately predict H_2 adsorption in different kerogen types achieving the highest R^2 of 0.989 [50]. Overall, machine learning, empowered by its capacity to learn from datasets of accurate simulation and generalize to unseen data, emerges as a valuable approach for understanding and predicting complex fluid behaviors in large-scale porous media. However, machine learning based on direct simulation results has not yet been applied to the prediction of H_2 storage.

In this paper, an improved LBM is proposed to simulate H_2 density distribution in 3D kerogen and MMT nanoporous media under different pressures using the results derived from MS, and the adsorption behaviors in nanoporous media are discussed. Then, employing the watershed algorithm, the porous media are divided into 2538 pore structures. Subsequently, through the features of pore structures and their associated gas adsorption characteristics, a database is constructed to train an artificial neural network (ANN) for precise prediction of adsorption behaviors in arbitrary pore structures. Finally, utilizing the trained ANN, the H_2 adsorption in a real digital core comprising 5419 pore structures is predicted.

2. Methodology

2.1. Lattice Boltzmann method based on molecular simulation

To elucidate the improvement of gas recovery and carbon geological sequestration through the examination of CO_2/CH_4 competitive adsorption in nanoporous media, a single-relaxation-time pseudopotential LBM, by modifying the fluid-fluid and fluid-solid interaction force parameters from MS, was introduced to characterize the competitive adsorption phenomena in shale porous media in previous work [44,45]. However, the previous model is challenging to control the total gas content in each pore structure of porous media under varying temperature and pressure conditions, causing the simulated bulk density to deviate from the gas density under corresponding temperature and pressure. Therefore, it is imperative to conduct multiple simulations to ensure the accuracy of the simulation results, which consumes a lot of computing resources. In this paper, the above model is improved by incorporating a source term condition into the bulk region, ensuring that the bulk density remains equal to the gas density at the corresponding temperature and pressure to investigate the H_2 adsorption behaviors in this work. The governing equation of Shan-Chen LBM is defined as

$$f_{\sigma,\alpha}(\mathbf{x}+\mathbf{e}_\alpha\delta_t, t+\delta_t) - f_{\sigma,\alpha}(\mathbf{x},t) = -\frac{1}{\tau}\left[f_{\sigma,\alpha}(\mathbf{x},t) - f^{eq}_{\sigma,\alpha}(\mathbf{x},t)\right] \quad (1)$$

where $f_{\sigma,\alpha}$ is the density distribution representing H_2 in this paper, $\alpha = 0, 1, 2, \ldots, 18$ is the direction of D3Q19 mode, $\mathbf{x}$ is position, t is time, $\mathbf{e}_\alpha$ is unit velocity; δ_t is the time step; τ is the relaxation time; $f^{eq}_{\sigma,\alpha}$ is the equilibrium density distribution.

To characterize gas adsorption characteristics, the gas-solid interaction force $\mathbf{F}_{\sigma,\mathrm{ads}}$ is formulated by Eq. (2), and the variation trend of adsorption density distribution can be adjusted by the gas-solid force parameter $G_{\sigma s}$ and constant value $\lambda = 0.3$ nm. The gas-solid force parameter can be determined via MS, enabling accurate capture of intermolecular forces. Fig. 1 illustrates the MS results of H_2 density distribution in 5 nm slit pores under pressure conditions (3 MPa, 6 MPa, 9 MPa, 12 MPa, 15 MPa, 18 MPa), temperature (333.15 K) and mineral types (kerogen and MMT), as presented in Zhang's study [17]. Based on the MS density distribution, the H_2 content within the slit pores is initially determined. Subsequently, the gas-solid force parameter $G_{\sigma s}$ is adjusted to match the MS density distribution. The fitting results are depicted in Fig. 1, illustrating a precise alignment between the bulk density obtained via LB simulation and MS data. Detailed explanations

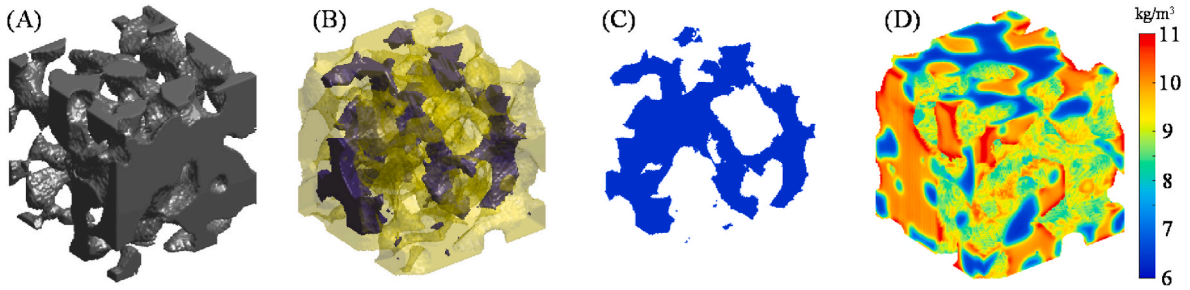

Fig. 2. LB simulation. (A) Solid matrix of porous media, (B) Pore space (yellow) and bulk space (gray), (C) Density distribution of bulk H_2, (D) Density distribution of H_2 in porous media. The cubic porous media have a physical side length of 20 nm.

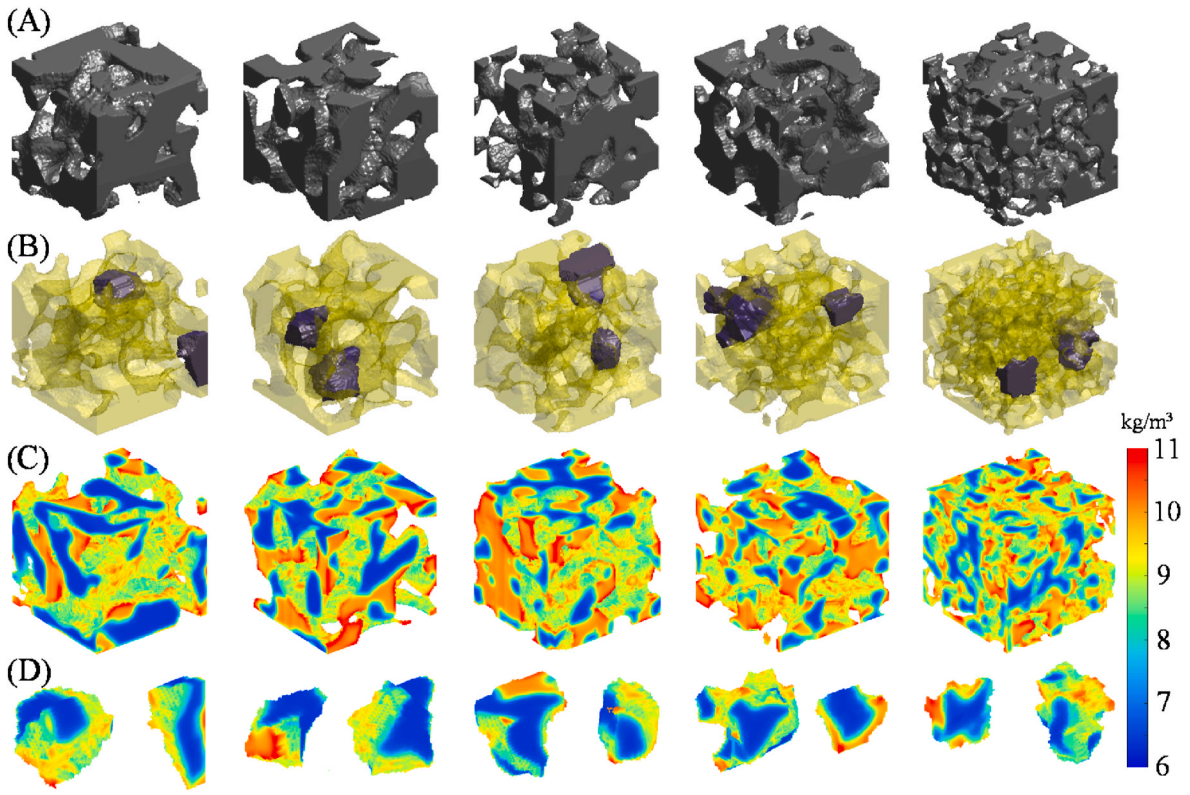

Fig. 3. Pore structure and H_2 density distribution in porous media. (A) Solid matrix, (B) pore space and two pore structures, (C) and (D) density distributions in kerogen porous media and pore structure at 9 MPa. Note: From left to right, the pore size of the porous media gradually decreases. The cubic porous media have a physical side length of 20 nm.

and principles regarding the fitting process can be found in our earlier publications [44].

$$\mathbf{F}_{\sigma,\mathrm{ads}}(\mathbf{x},t) = -G_{\sigma s}\left(1-\exp\left(\sum_{\alpha} f_{\sigma,\alpha}\right)\right)\sum_{\alpha} e^{-\mathbf{x}_\alpha\backslash\lambda}\mathbf{e}_\alpha \tag{2}$$

where $\mathbf{x}_\alpha$ is the distance from the solid in direction α at position $\mathbf{x}$.

In a single nanopore, the H_2 density at the corresponding temperature and pressure is feasible, yet achieving this precision becomes challenging when dealing with porous media characterized by complex pore structures [44]. In this paper, a source term is introduced to modulate the H_2 density within the bulk region away from solid wall, enabling a precise simulation of H_2 adsorption behavior across varying temperatures and pressures, as given in Eq. (3). The bulk region of the porous media is initially determined (Fig. 2A and B), with this designated bulk region representing the gas density inside that remains unaffected by interaction forces with solid walls. Subsequently, during the LB simulation, the density of the bulk H_2 remains consistent with the H_2 density dictated by the respective temperature and pressure (Fig. 2C), with adjustments made to the density distribution function $f_{\sigma,\alpha}$ at the edge of the bulk region at each cycle step. Finally, the density distribution corresponding to the designated temperature and pressure conditions is depicted in Fig. 2D.

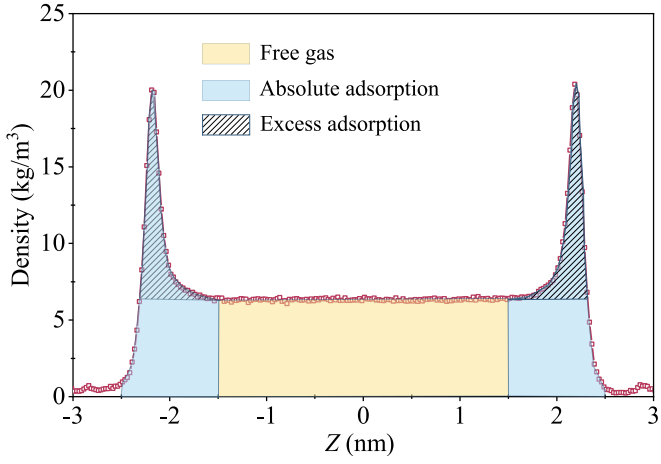

Fig. 4. Characterization of free gas, absolute adsorption, and excess adsorption derived from the density distribution obtained through MS.

$$f_{b,\sigma,\alpha} = f'_{b,\sigma,\alpha}\frac{\rho_b}{\sum_\alpha f'_{b,\sigma,\alpha}} \tag{3}$$

where ρ_b is the density at the corresponding temperature and pressure, approximately 2.14 kg/m^3, 4.19 kg/m^3, 6.36 kg/m^3, 8.18 kg/m^3, 10.05 kg/m^3, 11.79 kg/m^3 under the pressures 3 MPa, 6 MPa, 9 MPa, 12 MPa, 15 MPa, 18 MPa and temperature (333.15 K), respectively, $f'_{b,\sigma,\alpha}$ is the density distribution function of the bulk phase region post-migration, $f_{b,\sigma,\alpha}$ is the density distribution function modified by source term which can be used for subsequent interaction force calculations and collisions.

2.2. Database for machine learning

The idea of machine learning in this paper is to predict the H_2 mass in arbitrary pore structures, and subsequently deduce the occurrence characteristics of H_2 in the porous media by superimposing all pore structures. Consequently, it necessitates the establishment of a one-to-one correspondence database linking pore structures with their respective H_2 masses. Firstly, 40 3D kerogen and MMT porous media are constructed, respectively [51–53], with select examples depicted in

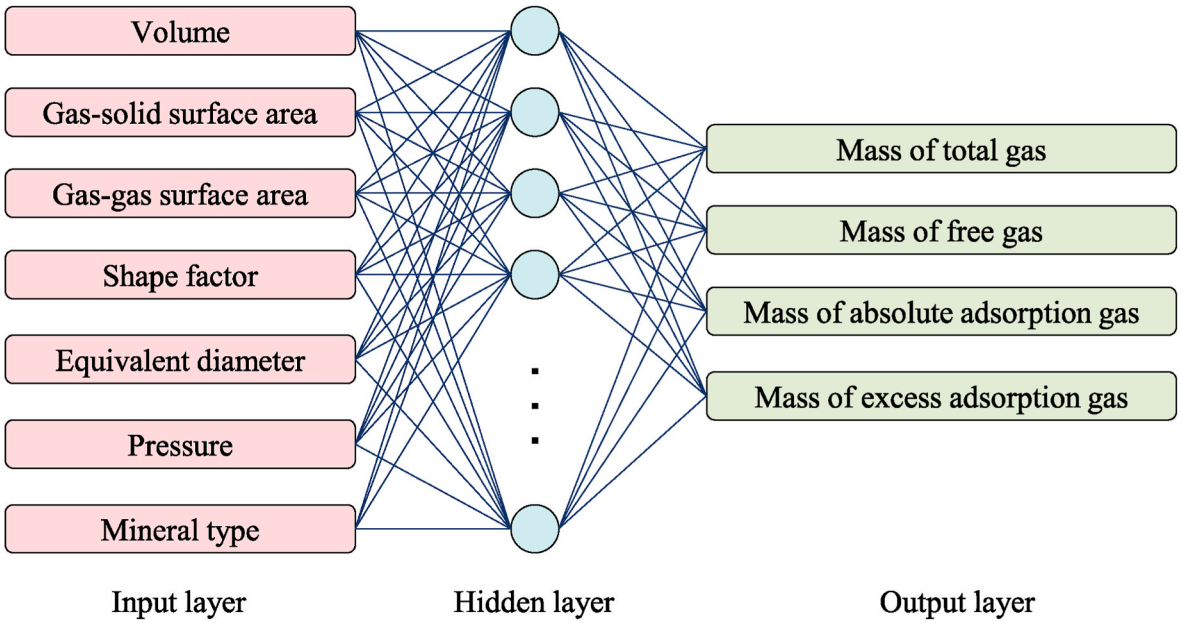

Fig. 5. Schematic diagrams of neural network with 1 hidden layer.

Fig. 3A. The lattice size is 100 × 100 × 100, and the corresponding physical size is 20 × 20 × 20 nm^3. Subsequently, 2538 pore structures are extracted from pore space utilizing the watershed algorithm, and representations of the pore space along with several pore structures are provided in Fig. 3B. The pore structure features, including the volume, gas-solid surface area, gas-gas surface area, shape factor and equivalent pore diameter, are calculated. The volume V_p delineated as the grid volume. The gas-solid surface area S_{gs} represents the area where H_2 is in contact with the pore wall. Conversely, the gas-gas surface area S_{gg} denotes the surface area where the pore structure is in contact with other

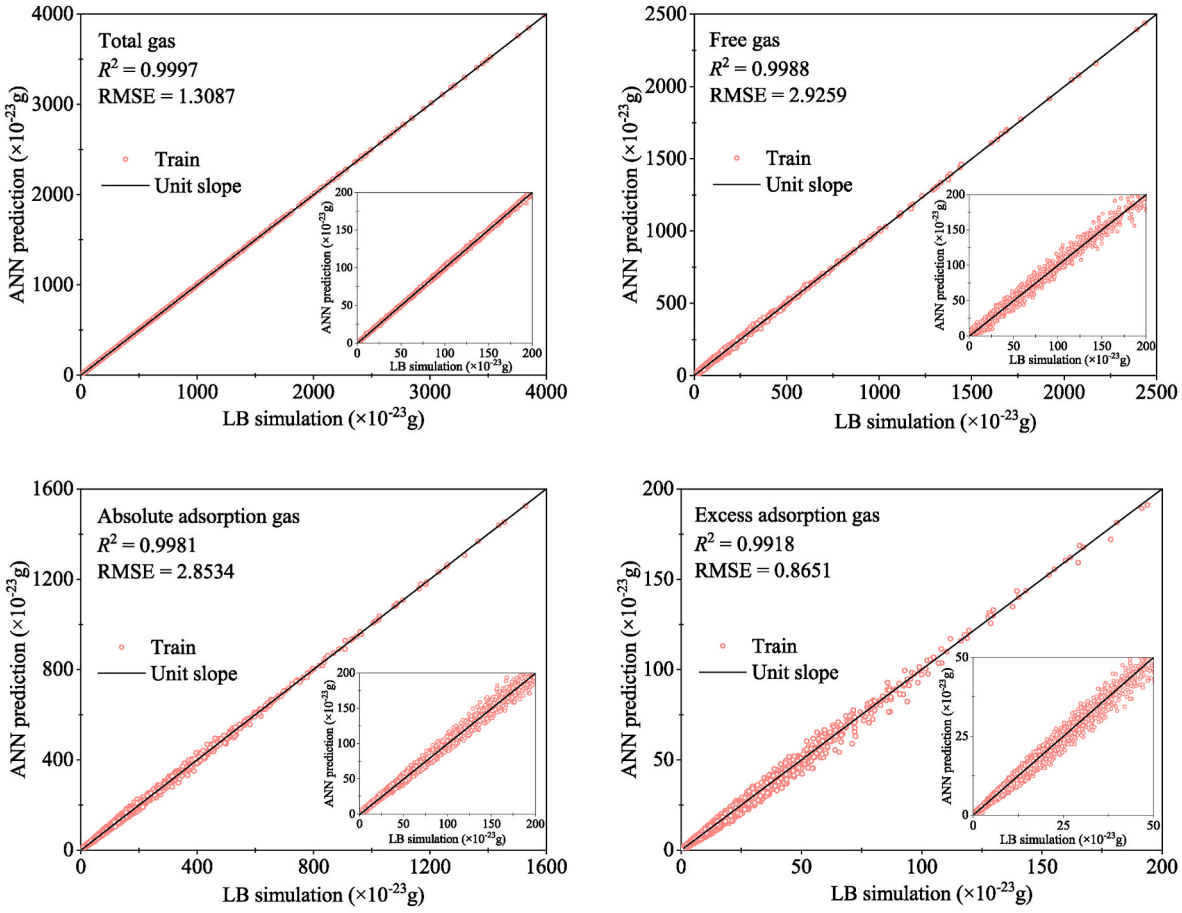

Fig. 6. The comparison of the mass of different types of H_2 between ANN prediction and LB simulation.

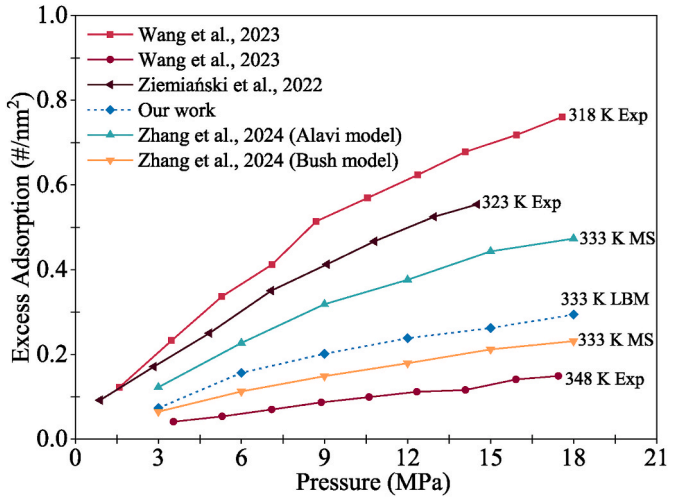

Fig. 7. The comparison of the excess adsorption of H_2 between experimental measurement, MS calculation and LB simulation, # is the molecular number [17,54–57].

pore structures. The shape factor is determined by the formula $\left(S_{gg}+S_{gs}\right)^3/\left(36\pi V_p^2\right)$. The equivalent pore diameter is calculated by the formula $2\sqrt[1/3]{3V_p/4}$.Then, utilizing the fitted gas-solid force parameter $G_{\sigma s}$, the adsorption characteristics of H_2 in the kerogen and MMT porous media are simulated via LBM under 6 distinct pressures. The density distributions in porous media are illustrated in Fig. 3C. Finally, through the density distribution in each pore structure as depicted in Fig. 3D, the mass of total, free, absolute adsorption and excess adsorption H_2 in each pore structure can be statistically derived. The classification of H_2 is visualized in Fig. 4. The physical mass M_p utilized in the subsequent analyses can be calculated using the length scale $L_0 = 2\times\ 10^{-10}$ m, mass scale $M_0 = 8\times10^{-27}$ kg and lattice mass M_l. Based on the H_2 density ρ_l at a grid point, the physical density can be calculated as $\rho_p = \rho_l\frac{M_0}{L_0^3}$, then, the physical mass of H_2 at a grid point is given by $M_p = \rho_p L_0^3$. Considering 6 pressure conditions and 2 mineral types, a total of 30456 sets of data can be collected for subsequent machine learning aimed at predicting H_2 mass across arbitrary pressures, minerals, and pore structures.

2.3. Neural network prediction

The ANN, illustrated in Fig. 5, is applied to predict the H_2 occurrence state in arbitrary pore structure. The input layer is composed of 7 characteristic parameters (the volume, gas-solid surface area, gas-gas surface area, shape factor, equivalent pore diameter, pressure and mineral type), while the output layer consists of 4 parameters (mass of total, free, absolute adsorption and excess adsorption gas). The hidden layer comprises 25 modes, and the 5-fold cross validation method is employed to evaluate the accuracy. The comparisons of the mass of different types of H_2 between ANN prediction and LB simulation are depicted in Fig. 6. The high coefficient of determination R^2 (>0.99) and small root mean square error (RMSE) indicated the ANN, based on the large-size database, is capable of accurately predicting the H_2 mass in the arbitrary pore structure. The flowchart of the methodology can be found in Fig. A1 in Appendix A.

2.4. Validation with experiments and MS

The excess adsorption behaviors measured by experiments and calculated using MS are employed to verify the excess adsorption in porous media simulated by LBM. Based on the total excess adsorption amount and gas-solid surface area in 2538 pore structures of 40 MMT porous media, the molecular number of excess adsorbed H_2 per nm^2 (Γ_{ex}) can be calculated by

$$\Gamma_{ex} = \frac{\int_{|y|=0}^{N_t}\left(\rho_l\frac{M_0}{L_0^3}-\rho_b\right)L_0^3 dyN_A}{M_H S_{gs-t}L_0^2} \tag{4}$$

where N_t is the total number of grids occupied by H_2, $N_A = 6.02\times10^{23}$ is Avogadro's constant, $M_H = 2$ g/mol is the molar mass of H_2, S_{gs-t} is the total surface area of 2538 pore structures of 40 porous media. As shown in Fig. 7, the results show that the simulated excess adsorption falls well within the range of published data. Thus, the methodology can be applied to simulate, train, and predict H_2 storage in porous media.

3. Results and discussion

3.1. Adsorption behaviors in porous media

Based on the H_2 density distribution in 40 porous media under 6

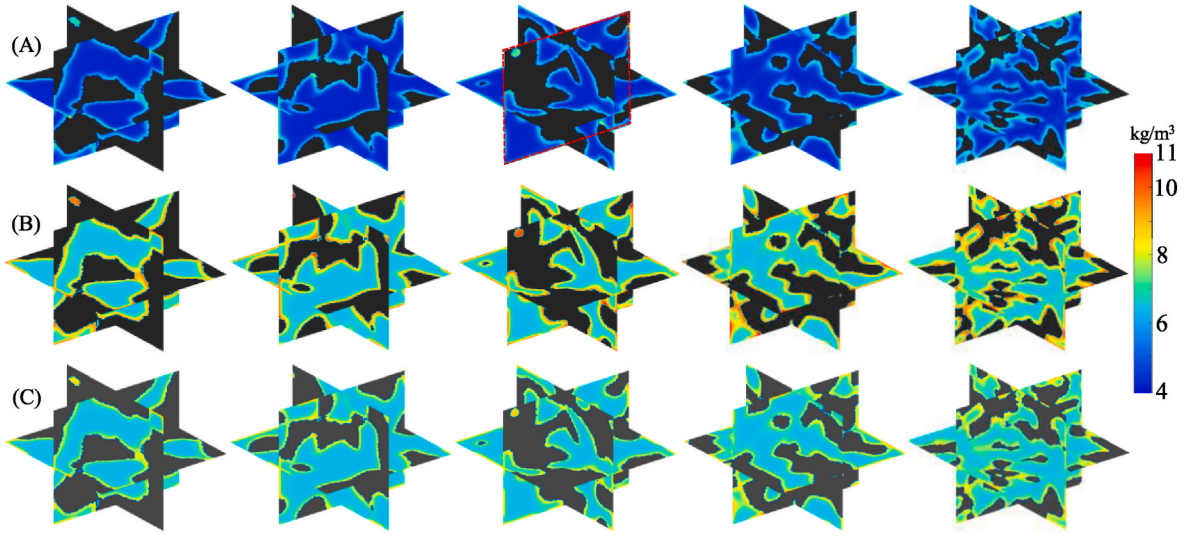

Fig. 8. Density distribution in kerogen and MMT porous media under various pressures. (A) Kerogen porous media at 6 MPa, (B) kerogen porous media at 9 MPa, (C) MMT porous media at 9 MPa. Note: From left to right, the pore size of the porous media gradually decreases. The cubic porous media have a physical side length of 20 nm.

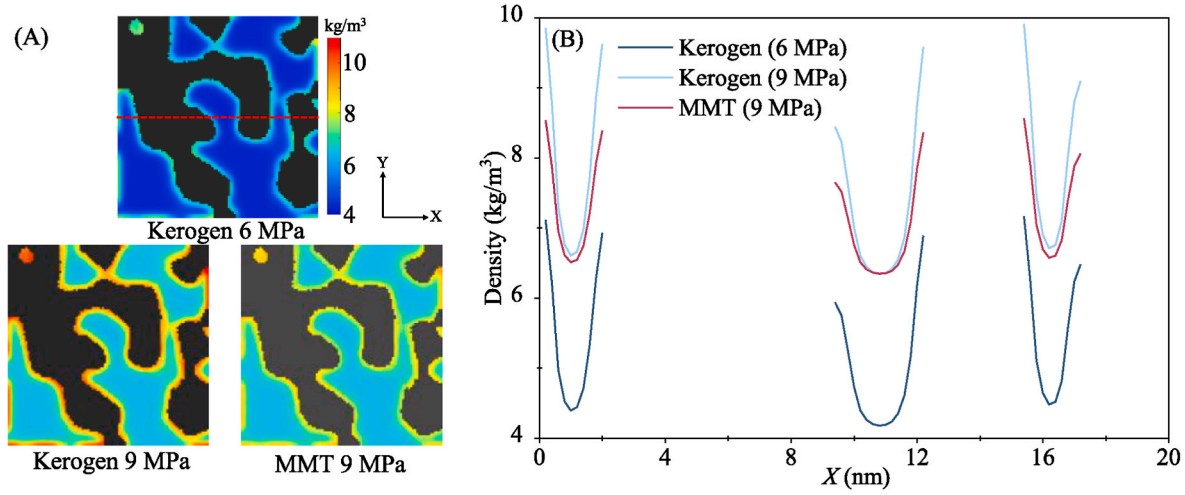

Fig. 9. Density distribution (A) and density distribution curve (B) of H_2 in kerogen and MMT porous media. The 2D porous media are a slice of 3D porous media, as shown by the red dashed line area in Fig. 8. The density distribution curve is at the central axis of the porous media, as shown by the red dashed line. *X* denotes the distance from the left boundary of the porous media. The square porous media have a physical side length of 20 nm.

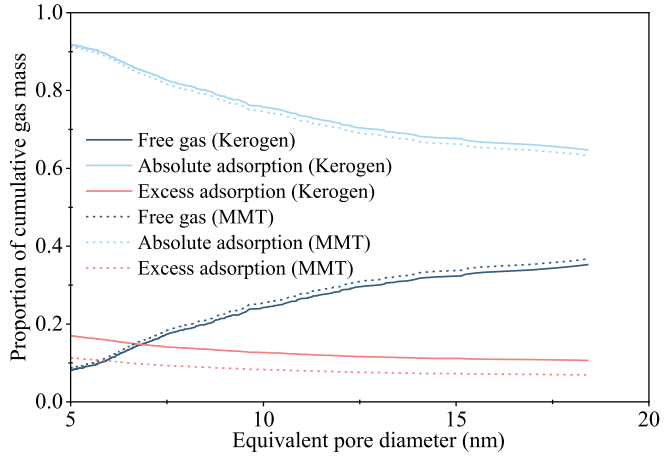

Fig. 10. Proportion of cumulative gas mass for free, absolute adsorption and excess adsorption H_2 versus equivalent pore diameter at 9 MPa.

pressure conditions and 2 mineral types, the occurrence characteristics of H_2 in various pore structures are analyzed. Fig. 8 illustrates the H_2 density distribution in kerogen and MMT porous media with pressure equaling 6 MPa and 9 MPa. The density distribution of a slice of 3D porous media and the corresponding density distribution curve along the central axis of the slice are shown in Fig. 9. As pressure increases, the density of adsorbed H_2 markedly increases. Furthermore, the density of adsorbed H_2 in kerogen porous media exceeds that in MMT porous media. Subsequently, the cumulative mass of total, free, absolute adsorption, and excess adsorption H_2 in specific equivalent pore diameter is calculated based on the different occurrence characteristics of H_2 in each pore structure. The calculation of cumulative mass is defined as the sum of gas masses in pore structures with an equivalent pore diameter smaller than the specified equivalent pore diameter. Fig. 10 illustrates the effect of equivalent pore diameter on the proportion of the cumulative gas mass for free, absolute adsorption and excess adsorption H_2. Due to the constant thickness of adsorbed layer, the proportion of the adsorbed phase volume relative to the total volume of pore structure decreases as the equivalent pore diameter increases. Consequently, the proportion of cumulative gas mass for absolute adsorption and excess adsorption H_2 decreases, whereas the proportion for free H_2 increases. The proportion of cumulative gas mass for absolute adsorption and excess adsorption H_2 in kerogen porous media is greater than in MMT porous media. Additionally, the cumulative mass of H_2 varies with pressure, mineral type and occurrence type, as shown in Fig. 11. The findings reveal a correlation between the cumulative mass of excess adsorption H_2 and pressure, demonstrating an increase as the pressure increases. Owing to the greater adsorption tendencies in kerogen, there is an increase in the cumulative mass of total, absolute adsorption and

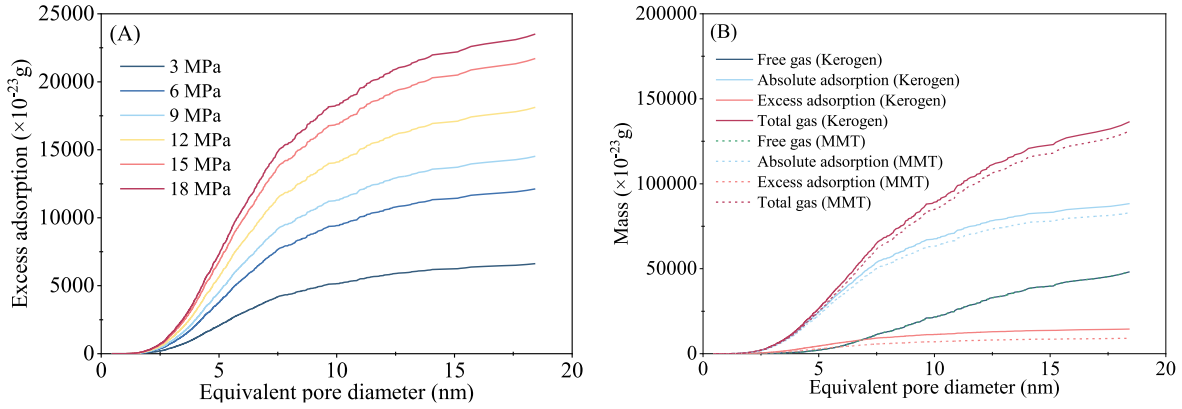

Fig. 11. Variation of accumulated H_2 mass with pore diameter. (A) Different pressures in kerogen pores, and (B) Different types of H_2 in kerogen and MMT pores at 9 MPa.

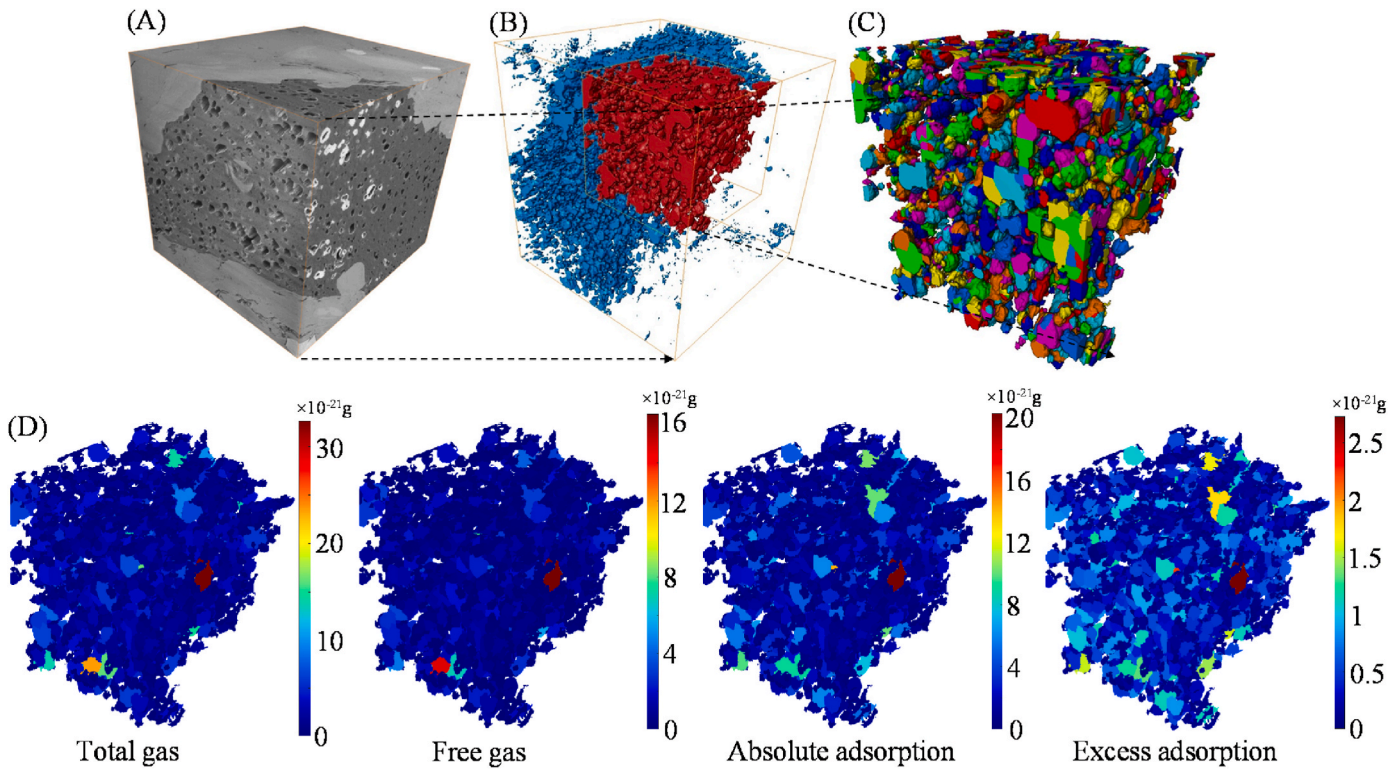

Fig. 12. Prediction of H_2 mass in a real kerogen pore structure at 3 MPa (The size of porous media is 9850 × 10900 × 9900 nm^3). (A) Reconstructed samples via FIB-SEM, (B) extracted pore space, (C) pore structures divided by the watershed algorithm, (D) prediction of the mass of total, free, absolute adsorption and excess adsorption H_2 (The cubic porous media have a physical side length of 200 nm).

excess adsorption H_2. These observations align with the outcomes of MS conducted on single nanopores [17], suggesting that the scaling up of single nanopore to porous media simulations is achievable by determining the pore-scale simulation parameters through MS.

3.2. Prediction based on real digital core

The true pore structures from Sichuan Basin, southwest China, as depicted in Fig. 12A and B, were obtained using the focused ion beam-scanning electron microscopy (FIB-SEM) technique, offering a resolution of 10 nm with an average pore diameter of approximately 100 nm, and the size of porous media is 9850 × 10900 × 9900 nm^3 [58]. The selected kerogen region in the upper right corner serves as the digital core structure for subsequent predictions. With a lattice size is 500 × 500 × 500, simulating H_2 storage behavior using pore-scale simulations demands significant computational resources. However, leveraging the ANN discussed above, the H_2 storage state in this kerogen digital core structure can be efficiently predicted.

In nanoscale pores, the thickness of the H_2 adsorption region is about 1.5 nm according to the layered density distribution from MS [17]. As the pore diameter increases, the influence of excess adsorption gas on the H_2 occurrence gradually diminishes and approaches 0. Therefore, the H_2 storage prediction is mainly conducted for the pore diameter of less than 20 nm in this paper. Currently, fractal theory is employed to characterize the characteristics of porous media and pore structures, indicating self-similarity characteristics across different scales and sizes [59–61]. Consequently, assuming similarity in pore structure features across different equivalent pore diameters in reservoirs, the obtained pore structure with a resolution of 10 nm is downscaled to 0.4 nm. This results in a corresponding physical size of the kerogen digital core with the lattice number 500 × 500 × 500 being 200 × 200 × 200 nm^3. As illustrated in Fig. 12C, the kerogen porous media is segmented into 5419 pore structures using the watershed algorithm, allowing for extraction of volume, surface area, and other characteristic parameters. Based on the characteristics of 5419 pore structures and the trained ANN, rapid prediction of H_2 storage can be quickly performed. The masses of total, free, absolute adsorption, and excess adsorption H_2 in each kerogen pore structure under a pressure of 3 MPa are depicted in Fig. 12D. By summing the mass of the gas in all pore structures, the masses of total, free, absolute adsorption, and excess adsorption H_2 in kerogen digital core are equal to 3.76 × 10^{-16} g, 1.11 × 10^{-16} g, 2.65 × 10^{-16} g and 0.67 × 10^{-16} g, and the mass of adsorbed gas accounted for 70.48% of the total gas mass.

4. Conclusions

This work develops a coupling method integrating MS, pore-scale simulations, and machine learning to simulate and predict the density distribution of H_2 in nanoporous media and to calculate the mass of total, free, absolute adsorption, and excess adsorption gas. Subsequently, the adsorption behaviors of H_2 in porous media and the mass of H_2 in a real digital core are analyzed. The main conclusions are as follows:

(1) An improved LBM, incorporating a source term condition into the bulk region, is established to enable precise simulation of gas density distribution in nanoporous media under specific temperature and pressure conditions. The gas-solid interaction parameters in the lattice Boltzmann model are then determined by fitting the density distribution obtained from MS.
(2) With increasing pressure, the density of adsorbed H_2 increases significantly, and the density of adsorbed H_2 in kerogen porous media is greater than in MMT porous media. As the equivalent pore diameter increases, the proportion of cumulative gas mass for absolute adsorption and excess adsorption H_2 decreases, while the proportion for free H_2 increases. Moreover, the cumulative

mass of excess adsorption H_2 demonstrates an increase with pressure. Due to the greater adsorption behaviors in kerogen, the cumulative mass of total, absolute adsorption, and excess adsorption H_2 increases.

(3) The watershed algorithm is utilized to extract 2538 pore structures from multiple nanoporous media. For each pore structure, the volume, surface area, shape factor, and equivalent diameter are calculated, along with the gas mass contained within.

(4) Considering 6 pressures, 2 types of minerals (kerogen and montmorillonite) and 2538 pore structures, a comprehensive dataset comprising 30456 machine learning data sets is established. The ANN is successfully trained to predict the gas mass in arbitrary pore structure with a high coefficient of determination ($R^2 > 0.99$) and minimal RMSE. Leveraging this trained ANN, the H_2 storage in a real shale kerogen digital core with 5419 pore structures is predicted, and the masses of total, free, absolute adsorption, and excess adsorption H_2 in kerogen digital core are equal to 3.76×10^{-16} g, 1.11×10^{-16} g, 2.65×10^{-16} g and 0.67×10^{-16} g.

The methodology demonstrates universality and applicability, capable of accommodating various fluid adsorption behaviors in nanoscale environments, including shale oil/gas adsorption, CO_2 adsorption and permanent storage, and H_2 adsorption, which has significant implications for improving oil and gas recovery and supporting a green low-carbon economy. In general, this work mainly focuses on the storage stage of H_2, and does not consider the adsorption effects on H_2 release. During the recovery stage, a cushion gas is required to maintain the reservoir pressure during H_2 recovery, so the competitive adsorption of H_2 and cushion gas has an important impact on the recovery and purity of H_2 [16,17]. Meanwhile, there is primary water or fracturing fluid in shale nanopores [62,63], affecting gas adsorption and trapping gas through capillary force [7,64]. The proposed methodology can also be effectively extended to H_2-cushion gas miscible and gas-water immiscible systems.

CRediT authorship contribution statement

Han Wang: Writing – review & editing, Writing – original draft, Validation, Supervision, Software, Methodology, Investigation, Formal analysis, Conceptualization. **Ke Hu:** Writing – review & editing, Software, Methodology, Formal analysis. **Weipeng Fan:** Writing – original draft, Software, Investigation, Formal analysis, Data curation. **Mingshan Zhang:** Writing – review & editing, Writing – original draft, Software, Methodology, Investigation, Formal analysis. **Xuanzhe Xia:** Writing – original draft, Validation, Software, Methodology. **Jianchao Cai:** Writing – review & editing, Supervision, Software, Resources, Project administration, Methodology, Data curation.

Data availability

Data will be made available on request.

Declaration of competing interest

The authors declare that they have no known competing financial interests or personal relationships that could have appeared to influence the work reported in this paper.

Acknowledgment

This study was supported by the National Natural Science Foundation of China (52404048, 42172159), China Postdoctoral Science Foundation (2023M733872), Postdoctoral Fellowship Program of CPSF (GZB20230864), Science Foundation of China University of Petroleum, Beijing (No. 2462023XKBH009).

Appendix A. Flow chart of methodology

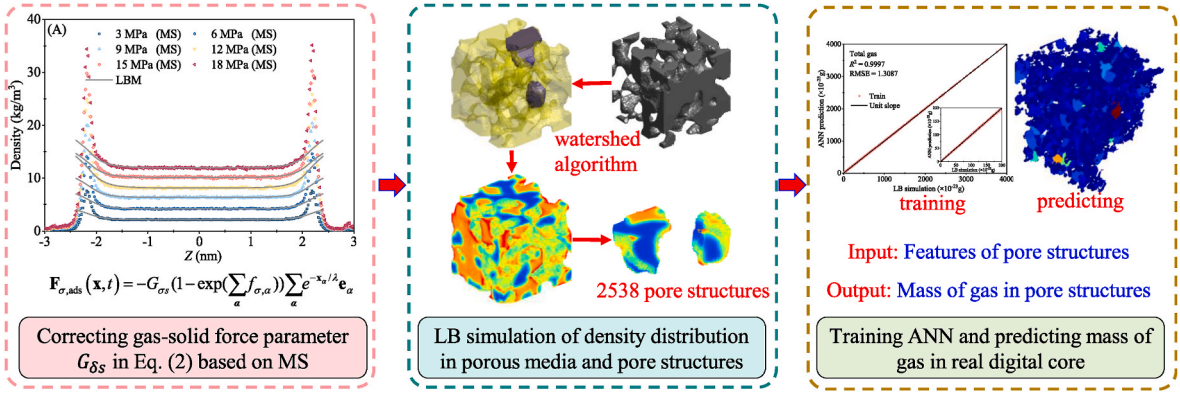

Fig. A1. Flow chart of methodology. The explanations of figures and formula can be found in the body of this article.

References

[1] Kumar S, Foroozesh J, Edlmann K, Rezk MG, Lim CY. A comprehensive review of value-added CO_2 sequestration in subsurface saline aquifers. J Nat Gas Sci Eng 2020;81:103437.

[2] Mouli-Castillo J, Heinemann N, Edlmann K. Mapping geological hydrogen storage capacity and regional heating demands: an applied UK case study. Appl Energy 2021;283:116348.

[3] Commission E. The European green deal. European Commission; 2019. p. 640. COM(2019).

[4] Tashie-Lewis BC, Nnabuife SG. Hydrogen production, distribution, storage and power conversion in a hydrogen economy-a technology review. Chem Eng J Adv 2021;8:100172.

[5] Ozarslan A. Large-scale hydrogen energy storage in salt caverns. Int J Hydrogen Energy 2012;37:14265–77.

[6] Sáinz-García A, Abarca E, Rubí V, Grandia F. Assessment of feasible strategies for seasonal underground hydrogen storage in a saline aquifer. Int J Hydrogen Energy 2017;42:16657–66.

[7] Al-Yaseri A, Yekeen N, Mahmoud M, Kakati A, Xie Q, Giwelli A. Thermodynamic characterization of H_2-brine-shale wettability: implications for hydrogen storage at subsurface. Int J Hydrogen Energy 2022;47:22510–21.

[8] Kanaani M, Sedaee B, Asadian-Pakfar M, Gilavand M, Almahmoudi Z. Development of multi-objective co-optimization framework for underground hydrogen storage and carbon dioxide storage using machine learning algorithms. J Clean Prod 2023;386:135785.

[9] Hematpur H, Abdollahi R, Rostami S, Haghighi M, Blunt M. Review of underground hydrogen storage: concepts and challenges. Adv Geo-Energy Res 2023;7:111–31.

[10] Muhammed NS, Haq B, Al Shehri D. CO_2 rich cushion gas for hydrogen storage in depleted gas reservoirs: insight on contact angle and surface tension. Int J Hydrogen Energy 2024;50:1281–301.

[11] Feng X, Liu J, Shi J, Hu P, Zhang T, Sun S. Phase equilibrium, thermodynamics, hydrogen-induced effects and the interplay mechanisms in underground hydrogen storage. Comput Energy Sci 2024;1:46–64.

[12] Wu L, Hou Z, Luo Z, Fang Y, Huang L, Wu X, et al. Impacts of microbial interactions on underground hydrogen storage in porous media: a comprehensive review of experimental, numerical, and field studies. Petrol Sci 2024. https://doi.org/10.1016/j.petsci.2024.08.015. in press.

[13] Bechara E, Gamadi T, Hussain A, Emadibaladehi H. Effect of hydrogen exposure on shale reservoir properties and evaluation of hydrogen storage possibility in depleted unconventional formations. Unconventional resources technology conference, 20–22 june 2022. Unconventional Resources Technology Conference (URTeC); 2022. p. 1734–48.

[14] Chen F, Mehana M, Nasrabadi H. Molecular simulation of hydrogen-shale gas system phase behavior under multiscale conditions: a molecular-level analysis of hydrogen storage in shale gas reservoirs. Energy Fuels 2023;37:2449–56.

[15] Al-Yaseri A, Amao A, Fatah A. Experimental investigation of shale/hydrogen geochemical interactions. Fuel 2023;346:128272.

[16] Liu K, Zhu W, Pan B. Feasibility of hydrogen storage in depleted shale gas reservoir: a numerical investigation. Fuel 2024;357:129703.

[17] Zhang M, Yang Y, Pan B, Liu Z, Jin Z, Iglauer S. Molecular simulation on H_2 adsorption in nanopores and effects of cushion gas: implications for underground hydrogen storage in shale reservoirs. Fuel 2024;361:130621.

[18] Ho TA, Dang ST, Dasgupta N, Choudhary A, Rai CS, Wang Y. Nuclear magnetic resonance and molecular simulation study of H_2 and CH_4 adsorption onto shale and sandstone for hydrogen geological storage. Int J Hydrogen Energy 2024;51:158–66.

[19] Liu J, Yao Y, Liu D, Elsworth D. Experimental evaluation of CO_2 enhanced recovery of adsorbed-gas from shale. Int J Coal Geol 2017;179:211–8.

[20] Pan B, Yin X, Ju Y, Iglauer S. Underground hydrogen storage: influencing parameters and future outlook. Adv Colloid Interface Sci 2021;294:102473.

[21] Lu C, Xiao X, Xue Z, Chen Z, Dong Y, Feng Y, et al. Investigations of methane adsorption characteristics on marine-continental transitional shales and gas storage capacity models considering pore evolution. Petrol Sci 2024;21:2273–86.

[22] Liu J, Xie L, Elsworth D, Gan Q. CO_2/CH_4 competitive adsorption in shale: implications for enhancement in gas production and reduction in carbon emissions. Environ Sci Technol 2019;53:9328–36.

[23] Klewiah I, Berawala DS, Walker HCA, Andersen PØ, Nadeau PH. Review of experimental sorption studies of CO_2 and CH_4 in shales. J Nat Gas Sci Eng 2020;73:103045.

[24] Abid HR, Yekeen N, Al-Yaseri A, Keshavarz A, Iglauer S. The impact of humic acid on hydrogen adsorptive capacity of eagle ford shale: implications for underground hydrogen storage. J Energy Storage 2022;55:105615.

[25] Alanazi A, Abid HR, Usman M, Ali M, Keshavarz A, Vahrenkamp V, et al. Hydrogen, carbon dioxide, and methane adsorption potential on Jordanian organic-rich source rocks: implications for underground H_2 storage and retrieval. Fuel 2023;346:128362.

[26] Wang C, Zhao Y, Wu R, Bi J, Zhang K. Shale reservoir storage of hydrogen: adsorption and diffusion on shale. Fuel 2024;357:129919.

[27] Singh H. Hydrogen storage in inactive horizontal shale gas wells: techno-economic analysis for Haynesville shale. Appl Energy 2022;313:118862.

[28] Babatunde KA, Negash BM, Mojid MR, Ahmed TY, Jufar SR. Molecular simulation study of CO_2/CH_4 adsorption on realistic heterogeneous shale surfaces. Appl Surf Sci 2021;543:148789.

[29] Raza A, Mahmoud M, Alafnan S, Arif M, Glatz G. H_2, CO_2, and CH_4 adsorption potential of kerogen as a function of pressure, temperature, and maturity. Int J Mol Sci 2022;23:12767.

[30] Zhang M, Liu Z, Pan B, Iglauer S, Jin Z. Molecular simulation on CO_2/H_2S co-adsorption in organic and inorganic shale nanopores. Appl Surf Sci 2023;624:157167.

[31] Wang F, Xu H, Liu Y, Meng X, Liu L. Mechanism of low chemical agent adsorption by high pressure for hydraulic fracturing-assisted oil displacement technology: a study of molecular dynamics combined with laboratory experiments. Langmuir 2023;39:16628–36.

[32] Cai J, Jiao X, Wang H, He W, Xia Y. Multiphase fluid-rock interactions and flow behaviors in shale nanopores: a comprehensive review. Earth-Sci Rev 2024:104884.

[33] Wang S, Chen F, Wu Y-S, Nasrabadi H. The potential of hydrogen storage in depleted unconventional gas reservoirs: a multiscale modeling study. Int J Hydrogen Energy 2023;48:16007–19.

[34] Raza A, Glatz G, Alafnan S, Mahmoud M, Gholami R. Depleted shale gas formations as naturally-occurring storage compartments for hydrogen: a molecular-level assessment. Fuel 2023;334:126695.

[35] Deng X, Zhang Q, Zhang Z, Li Q, Liu X. Adsorption and diffusion behavior of CO_2/H_2 mixture in calcite slit pores: a molecular simulation study. J Mol Liq 2022;346:118306.

[36] Shang Z, Yang Y, Zhang L, Sun H, Zhong J, Zhang K, et al. Hydrogen adsorption and diffusion behavior in kaolinite slit for underground hydrogen storage: a hybrid GCMC-MD simulation study. Chem Eng J 2024;487:150517.

[37] Wu Y, Tahmasebi P, Yu H, Lin C, Wu H, Dong C. Pore-scale 3D dynamic modeling and characterization of shale samples: considering the effects of thermal maturation. J Geophys Res: Solid Earth 2020;125:e2019JB018309.

[38] Zhang T, Luo S, Zhou H, Hu H, Zhang L, Zhao Y, et al. Pore-scale modelling of water sorption in nanopore systems of shale. Int J Coal Geol 2023;273:104266.

[39] Wang W, Xie Q, An S, Bakhshian S, Kang Q, Wang H, et al. Pore-scale simulation of multiphase flow and reactive transport processes involved in geologic carbon sequestration. Earth-Sci Rev 2023;247:104602.

[40] Chen L, He A, Zhao J, Kang Q, Li Z-Y, Carmeliet J, et al. Pore-scale modeling of complex transport phenomena in porous media. Prog Energy Combust Sci 2022;88:100968.

[41] Qin F, Fei L, Zhao J, Kang Q, Derome D, Carmeliet J. Lattice Boltzmann modelling of colloidal suspensions drying in porous media accounting for local nanoparticle effects. J Fluid Mech 2023;963:A26.

[42] Zhao J, Yao J, Zhang L, Sui H, Zhang M. Pore-scale simulation of shale gas production considering the adsorption effect. Int J Heat Mass Tran 2016;103:1098–107.

[43] Zhang T, Javadpour F, Li X, Wu K, Li J, Yin Y. Mesoscopic method to study water flow in nanochannels with different wettability. Phys Rev E 2020;102:013306.

[44] Wang H, Huang J, Zhan S, Zhang M, Cai J. Study on CO_2 and CH_4 competitive adsorption in shale organic and clay porous media from molecular- to pore-scale simulation. SPE J 2024;29:3265–76.

[45] Wang H, Zhang M, Xia X, Tian Z, Qin X, Cai J. Lattice Boltzmann prediction of CO_2 and CH_4 competitive adsorption in shale porous media accelerated by machine learning for CO_2 sequestration and enhanced CH_4 recovery. Appl Energy 2024;370:123638.

[46] Zhang T, Javadpour F, Li J, Zhao Y, Zhang L, Li X. Pore-scale perspective of gas/water two-phase flow in shale. SPE J 2021;26:828–46.

[47] Rabbani A, Babaei M. Hybrid pore-network and lattice-Boltzmann permeability modelling accelerated by machine learning. Adv Water Resour 2019;126:116–28.

[48] Jiang F, Yang J, Boek E, Tsuji T. Investigation of viscous coupling effects in three-phase flow by lattice Boltzmann direct simulation and machine learning technique. Adv Water Resour 2021;147:103797.

[49] Kang Q, Li K, Fu J, Liu Y. Hybrid LBM and machine learning algorithms for permeability prediction of porous media: a comparative study. Comput Geotech 2024;168:106163.

[50] Thanh HV, Dai Z, Du Z, Yin H, Yan B, Soltanian MR, et al. Artificial intelligence-based prediction of hydrogen adsorption in various kerogen types: implications for underground hydrogen storage and cleaner production. Int J Hydrogen Energy 2024;57:1000–9.

[51] Rabbani A, Jamshidi S. Specific surface and porosity relationship for sandstones for prediction of permeability. Int J Rock Mech Min Sci 2014;71:25–32.

[52] Rabbani A, Jamshidi S, Salehi S. An automated simple algorithm for realistic pore network extraction from micro-tomography images. J Petrol Sci Eng 2014;123:164–71.

[53] Rabbani A, Babaei M. Image-based modeling of carbon storage in fractured organic-rich shale with deep learning acceleration. Fuel 2021;299:120795.

[54] Wang L, Cheng J, Jin Z, Sun Q, Zou R, Meng Q, et al. High-pressure hydrogen adsorption in clay minerals: insights on natural hydrogen exploration. Fuel 2023;344:127919.

[55] Ziemiański PP, Derkowski A. Structural and textural control of high-pressure hydrogen adsorption on expandable and non-expandable clay minerals in geologic conditions. Int J Hydrogen Energy 2022;47:28794–805.

[56] Buch V. Path integral simulations of mixed para-D2 and ortho-D2 clusters: the orientational effects. J Chem Phys 1994;100:7610–29.

[57] Alavi S, Ripmeester J, Klug D. Molecular-dynamics study of structure II hydrogen clathrates. J Chem Phys 2005;123.

[58] Hu K, Liu Y, Zhang Q, Song Z, Thaika MA, Li R, et al. From micropores to macropores: investigating pore characteristics of longmaxi shale in the Sichuan Basin. Energy Fuels 2024;38(5):3961–81.

[59] Yu B, Li J. Some fractal characters of porous media. Fractals 2001;9:365–72.

[60] Cai J, Yu B, Zou M, Luo L. Fractal characterization of spontaneous co-current imbibition in porous media. Energy Fuels 2010;24:1860–7.

[61] Cai J, Zhang L, Wei W. Modelling of flow and transport in fractal porous media. Elsevier; 2020.

[62] Li J, Li X, Wu K, Feng D, Zhang T, Zhang Y. Thickness and stability of water film confined inside nanoslits and nanocapillaries of shale and clay. Int J Coal Geol 2017;179:253–68.

[63] Wijaya N, Sheng J. Effects of imbibition and compaction during well shut-in on ultimate shale oil recovery: a numerical study. SPE Reservoir Eval Eng 2021;24:859–73.

[64] Yang Y, Wan J, Li J, Zhu W, Zhao G, Shang X. Effects of impurity gases on interfaces of the hydrogen-water-decane three-phase system: a square gradient theory investigation. Capillarity 2023;9:9–24.